The Detection and Removal of Large-scale Detector Background Structures in NICMOS Observations

E. Y. Hsiao, N. Suzuki, P. Ripoche, G. Aldering, L. Faccioli, X. Huang,
S. Perlmutter, A. L. Spadafora, M. Strovink

Lawrence Berkeley National Laboratory

C. Lidman

Australian Astronomical Observatory

K. S. Dawson

University of Utah

L. E. Bergeron, S. Deustua, A. S. Fruchter

Space Telescope Science Institute

K. Barbary, H. K. Fakhouri, J. Meyers, D. Rubin

University of California, Berkeley

Abstract.   After applying the standard corrections for well-studied NICMOS anomalies, significant large-scale spatial background variation remains. We report on the detections of a sky-dependent fringe pattern in the F110W filter, and a time-dependent residual corner glow in the calibrated NICMOS deep science images. We also describe methods developed to further correct these anomalies. A model of the background structure is derived from the algebraic manipulation of stacked science images and consists of the following two components. The first component is constant, dominated by a residual glow as high as 20 DN at the corners and by residual flat and persistence structures at the center. The second component, which scales with sky level, displays a clear fringe pattern with 10% variation for F110W images. However this pattern is not detected for F160W images. Using these model components to correct for the anomalies significantly improves the cosmetic appearance of NICMOS images and reduces the magnitude scatter in the photometry of distant galaxies by 20%.

1   Introduction

The standard calibration pipeline `CALNICA` and additional STSDAS software have been excellent tools for observers, removing many of the well-studied NICMOS anomalies. Despite the aid of these tools, large-scale spatial background structures are still quite visible in the final calibrated deep images. These background structures cause variation as high as 60% in counts from the center to the corners. This makes the precision study of faint sources, which have counts near the sky level, exceptionally difficult. In this paper, we outline novel methods for deriving model images of the observed background structures and for removing them from individual images. We also present a technique for recovering the flux from the erratic middle column.

The data used for this study are deep NICMOS supernova follow up observations from the HST Cluster Supernova Survey (PI: Perlmutter) and the GOODS Transient Search (PI: Riess). The data are taken with NIC2 camera and F110W/F160W passbands between June, 2002 and August, 2008, after the installation of the NICMOS Cooling System. The data set contains 385 exposures in F110W and 188 exposures in F160W. The exposures are deep, typically ~ 1000 seconds of exposure time. They are also sparsely populated with distant faint sources, making them ideal for studying spatial background structures.

The science exposures are calibrated with the latest `CALNICA` pipeline (version 4.1.1; Dahlen et al. 2008) and STSDAS software `PEDSKY`. Exposures taken within one orbit of the last exit from the NICMOS SAA contour are put through the STSDAS software `SAACLEAN`, and corrections are made when needed. Four of our exposures suffer from significant bright earth persistence (BEP; Riess & Bergeron 2008), and are corrected using the STSDAS software `NIC_REM_PERSIST`.

2   Principal component analysis

Principal component analysis (PCA) is a powerful statistical technique which reduces the dimensionality and identifies patterns in a set of multi-dimensional data. PCA has been employed for analyzing astronomical data in a wide variety of applications (e.g., Suzuki 2006; Blanton & Roweis 2007). Here, we use PCA to characterize the intensity of the corner glow (Section 3) and to reconstruct the erratic middle column (Section 5).

The simplifying "bra ket" notation is adopted here for the formulation of PCA. For an n-dimensional data set $|f_i\rangle$ and its mean properties $|\mu\rangle$, the principal components (PCs) $|\xi_j\rangle$ are simply the eigenvectors of the covariance matrix for $|f_i - \mu\rangle$. The eigenvalue accounts for the variance of the data in the direction of the associated PC. When the PCs are ranked by their eigenvalues, the first PC points in the direction of maximum variance in the n-dimensional data space. The rest of the PCs are orthogonal vectors to the first: $\langle \xi_i | \xi_j \rangle = \delta_{ij}$.

The projection p_{ij} of $|f_i\rangle$ onto a PC $|\xi_j\rangle$ is computed as: $p_{ij} = \langle f_i - \mu | \xi_j \rangle$. The n-dimension data set can then be represented as the sum of all of its PCs:

$$|f_i\rangle = |\mu\rangle + \sum_{j=1}^{n} p_{ij} |\xi_j\rangle. \tag{1}$$

If the first few PCs constitute a large fraction of the overall variations, then they alone can provide decent reconstructions of the original data.

Here, we obtain the eigenvectors and eigenvalues of the covariance matrix using internal IDL routines which utilize Householder reductions and the QL method (Press et al. 1992). For the case where there is missing data (Section 5), we adopt the expectation maximum (EM; Roweis 1998) algorithm to obtain the PCs. The EM algorithm naturally accommodates missing data and allows for the extraction of only the first few leading PCs without having to diagonalize the entire covariance matrix.

3   Time dependence of residual corner glow

The most prominent large-scale background is the corner structure which resembles amplifier glow and linear dark current. Without understanding the origin of this structure, it is here loosely termed "residual corner glow." PCA (Section 2) is performed on the calibrated images to gain a better understanding of the shape and variation of this structure.

PCA is performed on calibrated and sky-subtracted images in absolute counts, with the center and sources masked out. The first PC (or eigen-image) has the shape of the corner glow and accounts for over half of the variation (Figure 1). The corner glow is thus not only prominent, but also varies between exposures. The eigen-images of the F110W

and F160W data sets show very similar characteristics, consistent with the orientation at the detector.
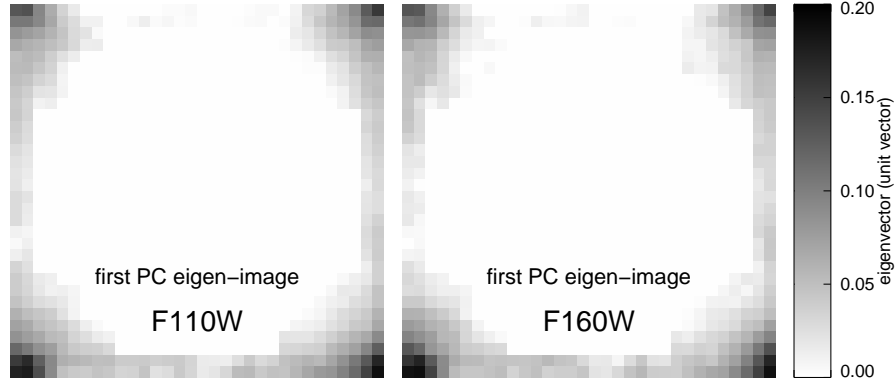

Figure 1: First PC eigen-image of the residual corner glow. The left and right panels show the eigen-images for the F110W and F160W data sets, respectively.

The projections of individual images onto the first PC eigen-image are used here as a measure of the corner glow intensity (Figure 2). They reveal that the intensity of the corner glow varies with time: starts high, decays exponentially, resets every orbit, but never goes to zero. This behavior may be the result of larger variation in detector temperature that cannot be accounted for by the bias temperature. At the beginning of the orbit, the detector is slightly warmer after spending the occultation in auto-flush. The high corner glow intensity can then be attributed to higher linear dark current, higher amplifier glow, and even persistence from the amplifier glow.

The intensity and the time evolution of the corner glow are quite uniform. For several consecutive exposures taken within an orbit, the behavior of exponential time decay is clear. However, most images in this data set have exposure times much larger than the *e*-folding time of the exponential decay. The intensity then appears binary in nature as shown in Figure 2. This allows the images to be segregated into two groups of approximately constant corner glow. With this simplification, we can devise a simple model of the background structure that can be extracted with algebraic manipulation of stacked images.

4 Deriving model images

The background structures are modeled as two components: 1) component G which is constant in absolute counts, and 2) component F which scales with the sky level. Component G is designed to capture the residual corner glow (Section 3). Segregating images according to the residual corner glow justifies the use of a constant component. The models are derived for each filter (F110W and F160W) and for each glow group (high and low). The sky-subtracted calibrated science image I in DN/s is then modeled as the sum of the contributions from the two background model components, G and F, in the following two ways:

$$t(I + s) = stF + G + tI_0,$$

$$t(I + s) = t(I_0 + s)F + G,$$

(2)

where I_0 denotes the desired zero-background image I_0 in DN/s, s denotes the sky level in DN/s, and t denotes the exposure time in seconds. To measure the sky level, we fit a Gaussian to the count histogram of the source-masked image before sky subtraction. The
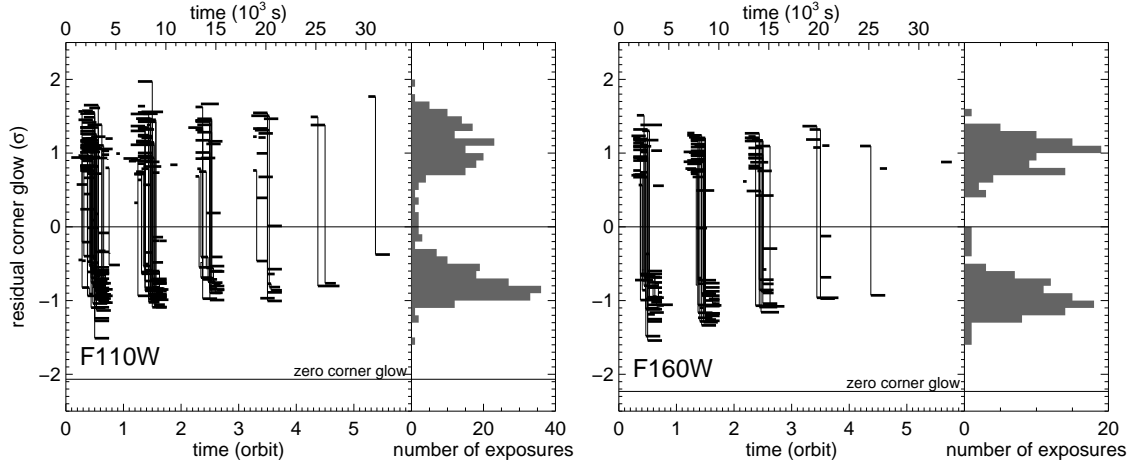
Figure 2: Time sequence of the residual corner glow intensity. The projections on the first PC are shown in the number of standard deviations away from the mean, and are used as a measure of the corner glow intensity. Each horizontal mark represents one exposure and its exposure time. Consecutive observations are connected with a vertical line. The left and right panels show the time sequence for the F110W and F160W data sets, respectively. Histograms are plotted to show the distribution of intensities. Note the uniformity of the intensity and that none of the exposures reaches zero.

Gaussian is truncated on the high side to avoid including the corner glow. The resulting sky levels agree well with the PEDSKY output of SKYVAL.

The model components, F and G, can be solved algebraically using stacked images, where the over-line average symbol denotes median values or median stacked images:

$$F = \overline{\frac{\overline{t(I+s)} - \overline{\overline{t(I+s)}}}{\overline{st} - \overline{\overline{st}}}},$$

$$G = \overline{t(I+s) - st\overline{F}}. \tag{3}$$

Both cases in Equation 2 yield the same solution for model components G and F. The resulting models (Figure 3) show that we have successfully separated out two unique background structures for components G and F from the stacked images. The models derived from the high and low glow level sets of images show the same structures. They differ only in the intensities of the G component and the signal-to-noise. The models derived from the F110W and F160W filters show identical structures for the G component. However, fringe pattern is detected in F110W and *not* in F160W (Figure 3).

Not surprisingly, the corner structure of the G component largely resembles amplifier glow and linear dark current (panel a of Figure 4), as it is the main background structure we are attempting to extract (Section 3). The nonzero component G suggests that the bias temperature used in the current NICMOS reduction pipeline cannot account for the observed variation. The residual flat structure in component G also points to a temperature effect (panel b of Figure 4). The center negative structure resembles the structures in BEP (panel c of Figure 4). Riess & Bergeron (2008) reported significant BEP in 5% of the NICMOS exposures in the SHOES program. Here, for the fact that the structure survives median stacking and that it is visible in the inspection of individual images, we conclude that residual BEP-like structure affects every exposure.

The F component of F110W shows very clear fringe pattern, but none is detected in that of F160W. The pattern is well described by a simple model of concentric ellipses (panel d of Figure 4). The ellipses are centered approximately at $[128, 28]$, tilted at $\sim \frac{\pi}{6}$
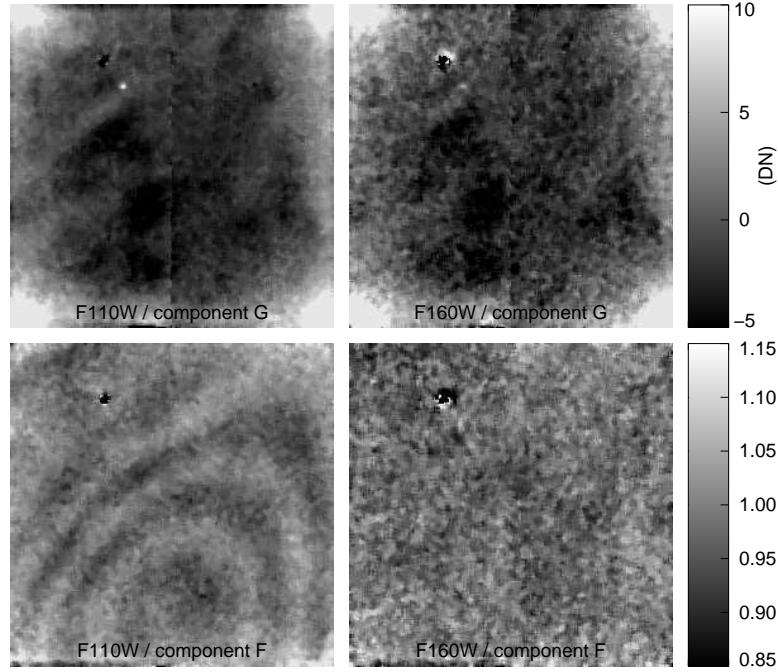
Figure 3: Model components for the background structure (available for download at `http://supernova.lbl.gov/~hsiao/nicmos/`). The left and right panels show model components from the F110W and F160W image sets, respectively. The top and bottom panels show component G which is constant in absolute counts and component F which scales with sky level, respectively.

with respect to the x axis, have minor radii in multiples of ~ 20 pixels and major-to-minor semi-axes ratio of ~ 1.5. The fringe pattern resembles neither the reference dark, flat (panel e of Figure 4) nor BEP (panel f of Figure 4). Fringe patterns in NICMOS have previously been reported in NIC1 narrow-band earth flats (Gilmore et al. 1998), but have never been reported for a wide filter. Gilmore et al. (1998) reported the effect to be particularly apparent in the bluest filters, F095N, F097N and F113N, and not detectable in the redder filters, F164N and F166N. These wavelength regions are consistent with our observation of fringing in F110W and non-detection in F160W, and suggest that only the bluest photons are affected by this anomaly.

It is unclear whether the observed fringe pattern in F110W is a result of true detector-induced fringing, although the characteristics of this structure seem to point in that direction. The fact that the structure does not resemble the reference files rules out a simple bias or color temperature effect. The ubiquity of the effect makes hypotheses such as stray light from optics and persistence less likely. The fact that the fringe structure scales with the sky and only affects the bluest photons gives clues to the source of the fringing photons. It is most likely zodiacal light which is blue at these wavelengths (Aldering 2002), although there are indications that bright earth limb could also be a factor. The interference rings are quite widely spaced; a mere sub-milliradian wedge in a detector layer can potentially produce such an effect. A model of the NIC2 detector layers with descriptions of index of refraction, transmission coefficient and thickness is required to confirm whether zodiacal light can indeed produce the observed pattern.
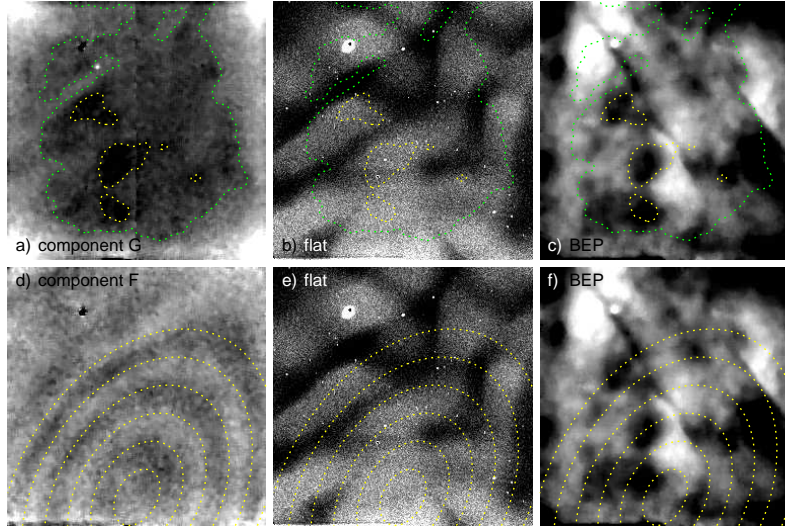
Figure 4: Comparisons between F110W model background structures and known NICMOS structures. The top panels compares component G (panel a) to reference flat (panel b) and BEP (panel c). The contour lines of component G are drawn at -4 (yellow) and -0.5 (green). The bottom panels compares component F (panel d) to reference flat (panel e) and BEP (panel f). The contour lines of component F are best fitting concentric ellipses at the scale of 1.

5 Reconstructing erratic middle rows and columns

The erratic middle row and column contain the first pixels read out in each quadrant. This anomaly is suspected to be the result of the steep and highly non-linear detector shading corrections (Thatte et al. 2009), making these pixels especially susceptible to changes in the detector environment. Nonetheless, there is no reason to believe that these pixels are less sensitive. In this section, we outline methods for recovering the flux in these pixels. An image with corrected middle row and column yields substantial improvements in the extraction of astronomical sources and in the construction of model images (Section 4).

The erratic middle row and column in calibrated science images have drastically different characteristics (Figure 5). The noise characteristics of the middle row and neighboring rows are identical. The residual corner glow, although weak in this region, is preserved in the middle row. The application of a simple constant offset determined from source-masked middle and neighboring rows will recover the flux.

The behavior of the middle column is more complex. Here, we introduce a novel method for reconstructing the middle column using PCA with missing data. PCA is performed here to determine the bases for the variations in the middle columns (Section 2). Specifically, we adopt the algorithm of EM PCA (Roweis 1998). The EM PCA naturally accommodates missing data, which in this case are masked-out astronomical sources. Warm and hot pixels are also identified and masked using multiple iterations of the EM algorithm.

The first two principal component eigenvectors derived are plotted in the right panel of Figure 5. The first eigenvector describes the broad overall shape of the middle column and accounts for most of the variation (80.2%). Interestingly, a middle column with shorter exposure time tends to have a stronger curve, but the shape does not correlate with the residual glow level (the time sequence in the orbit; Section 3). The correlation perhaps reflects the state of the detector at the time of read out. The second eigenvector describes the coherent modulating signal which produces the larger-than-normal noise levels.
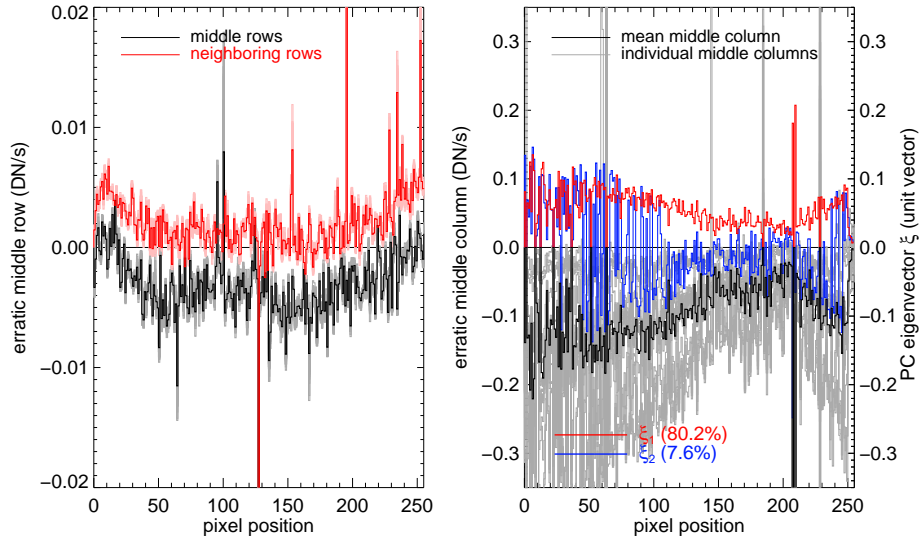
Figure 5: Comparison between the characteristics of erratic middle row and column. The left panel plots the median middle row in black and the median neighboring rows in red. The medians of bootstrapped samples for each case are plotted in the background to indicate the variability of the data. The right panel plots the mean middle column in black and individual middle columns in grey. The first two PCs eigenvectors are plotted in red and blue, describing the overall shape and the modulating signal of the middle columns, respectively.

A model middle column is custom-built for each image using the projections of each middle column (masked and reconstructed with the EM algorithm) onto the principal component eigenvectors. The number of eigenvectors included in the reconstruction is chosen to be the number of eigenvectors required to reach the noise level of neighboring pixels. Figure 6 illustrates an example of such a reconstruction.

6   Post-processing procedures and improvements

We summarize here the steps for deriving the two-component background model and for correcting individual exposures:

1. Construct masks from source extraction, data quality image and bad pixel map

2. Reconstruct erratic middle column and row of individual exposures

3. Segregate exposures using the intensity of residual corner glow

4. Derive model components from algebraic manipulations of stacked images

5. Fit model components to individual masked images

The construction of model images, recovery of the middle rows and columns, and the model fitting of individual exposures all require masks which exclude astronomical sources and defective pixels, while astronomical source extraction performs best on background-removed images. The above procedures thus need to be iterated. Here we use the `SExtractor` program (Bertin & Arnouts 1996) to build the catalog of all the sources for every image
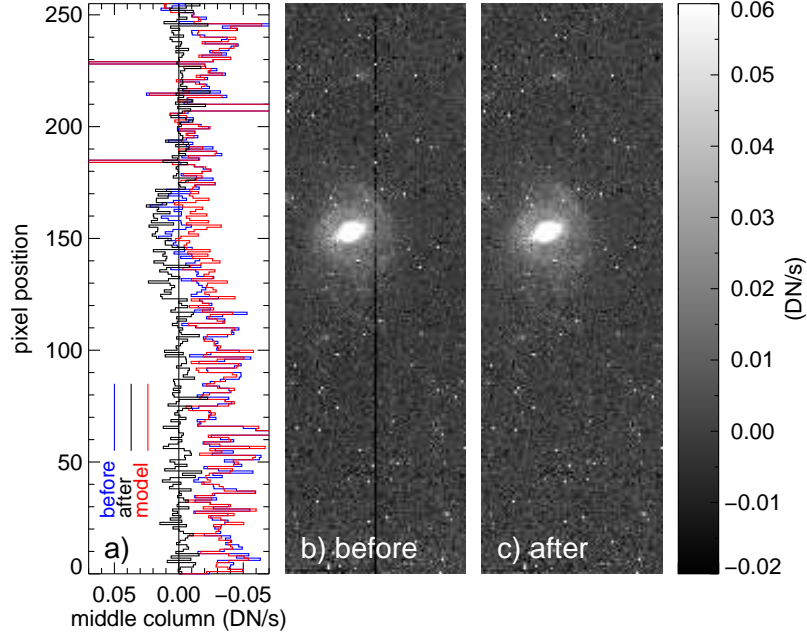
Figure 6: An example for the reconstruction of the middle column using PCA. Panel *a* plots the PCA reconstructed model in red, and the middle column before and after the correction in blue and black, respectively. Panels *b* and *c* show the images before and after the correction, respectively. The correction successfully recovers the galaxy flux.

and use the measured Petrosian radii to build the source mask. Also note that while the reconstructed middle row has the corner glow structure preserved, the reconstructed middle column does not (Section 5). The iterations thus also help obtain the characteristics of the corner structure for the extractions of gapless background models.

The two cases in Equation 2 can be written in terms of the desired zero-background image I_0 as follows:

$$I_0 = I - \left[s(F-1) + \frac{G}{t}\right],$$

$$I_0 = \frac{1}{F}\left(I - \left[s(F-1) + \frac{G}{t}\right]\right).$$

(4)

After obtaining the model images (Section 4), applying the corrections is trivial and the bulk of the background structure can be removed using Equation 4 with the sky value s and exposure time t for the image in question. Alternatively, since there is a spread in the intensities in the corner structures (Figure 2), fitting model components to individual masked images with variable sky value and exposure time can potentially improve the removal of the structures. Here we fit the model components using three free parameters: a fiducial sky value s', a fiducial exposure time t', and a constant offset. Non-linear least-squares IDL fitter `MPFIT` (Markwardt 2009), which adopts the efficient Levenberg-Marquardt technique, is used here to perform the fits. A typical example is illustrated in Figure 7.

The background-removed images have very obvious cosmetic improvement from the original calibrated images. To obtain a quantitative gauge of the improvement, we measure the dispersions in the fluxes of faint galaxies. Galaxies which appear in more than three images are included. The photometry adopted uses six-pixel radius apertures and local background subtraction. Median absolute deviation is adopted to provide a robust measure
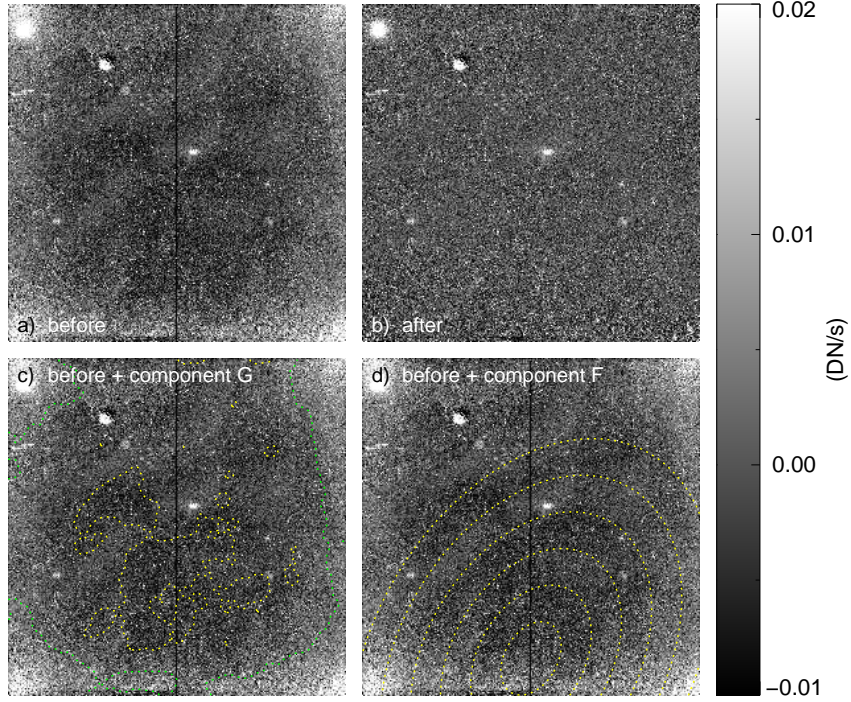
Figure 7: An example of the removal of background structures. Panels a and b show the example image before and after the removal of background structures, respectively. Panels c and d show the image before background removal with contours from the background model components G and F over-plotted, respectively. The contours for component G are -3 (yellow) and 3 (green) in DN. The contours for component F are concentric ellipses fitted at the scale of unity.
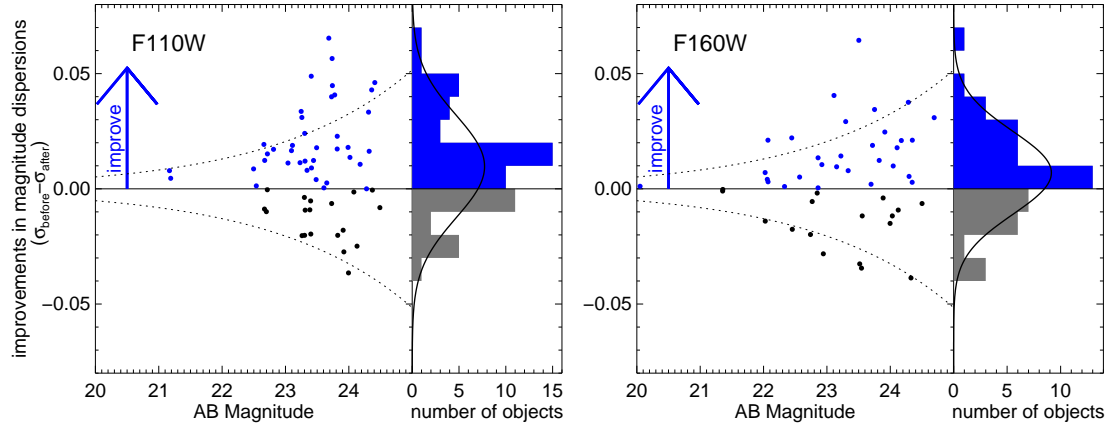

Figure 8: Improvements (reductions) in the magnitude dispersions for faint galaxies with respect to their average AB magnitude. The left and right panels plot the improvement for the F110W and F160W data sets, respectively. The first case of Equation 4 is applied here as an example. The dotted curves mark the expected magnitude dispersion from Poisson noise. The histograms and the best fit Gaussian functions show the distributions for both passbands shifted toward approximately 20% improvements.

of dispersion. Removing the background structures with the methods described here yields on average a 20% reduction of magnitude dispersion in the photometry of faint galaxies (Figure 8). The two methods of applying the corrections for component F from Equation 4 show similar improvements and no clear advantage for one over the other.

References

Aldering, G. 2002, "SNAP Sky Background at the North Ecliptic Pole," LBNL report LBNL-51157

Bertin, E., & Arnouts, S. 1996, A&AS, 117, 393

Blanton, M. R., & Roweis, S. 2007, AJ, 133, 734

Dahlen, T., McLaughlin, H., Laidler, V., Regan, M., Bergeron, L. E., Jedrzejewski, R., Bohlin, R., de Jong, R., & Viana, A. 2008, Instrument Science Report NICMOS 2008-002, 17 pages, 1

Gilmore, D., Ritchie, C., MacKenty, J., Colina, L., Bergeron, L. E., & Busko, I. 1998, Instrument Science Report NICMOS 1998-11, 10 pages, 1

Markwardt, C. B. 2009, Astronomical Society of the Pacific Conference Series, 411, 251

Press, W. H., Teukolsky, S. A., Vetterling, W. T., & Flannery, B. P. 1992, Cambridge: University Press, —c1992, 2nd ed.,

Riess, A., & Bergeron, E. 2008, Instrument Science Report NICMOS 2008-01, 14 pages, 1

Roweis, S. 1998, Neural Information Processing Systems 10, pp626-632

Suzuki, N. 2006, ApJS, 163, 110

Thatte, D., Dahlen, T., Barker, E., de Jong, R., Koekemoer, A., Pirzkal, N., Viana, A., & Wiklind, T. 2009, NICMOS Data Handbook, version 8.0, Baltimore, STScI